Inorganic Chemistry

Spectroscopic and DFT Investigation of [M{HB(3,5-^{i}Pr$_2$pz)$_3$}(SC$_6$F$_5$)] (M = Mn, Fe, Co, Ni, Cu, and Zn) Model Complexes: Periodic Trends in Metal–Thiolate Bonding

Serge I. Gorelsky,[†] Lipika Basumallick,[†] Josh Vura-Weis,[†] Ritimukta Sarangi,[†] Keith O. Hodgson,[†,‡] Britt Hedman,[‡] Kiyoshi Fujisawa,*[,§] and Edward I. Solomon*[,†]

Department of Chemistry, Stanford University, Stanford, California 94305, Stanford Synchrotron Radiation Laboratory, Stanford Linear Accelerator Center, Stanford University, Stanford, California 94309, and Department of Chemistry, University of Tsukuba, Tsukuba 305-8571, Japan

Received March 10, 2005

A series of metal-varied [ML(SC$_6$F$_5$)] model complexes (where L = hydrotris(3,5-diisopropyl-1-pyrazolyl)borate and M = Mn, Fe, Co, Ni, Cu, and Zn) related to blue copper proteins has been studied by a combination of absorption, MCD, resonance Raman, and S K-edge X-ray absorption spectroscopies. Density functional calculations have been used to characterize these complexes and calculate their spectra. The observed variations in geometry, spectra, and bond energies are interpreted in terms of changes in the nature of metal–ligand bonding interactions. The metal 3d–ligand orbital interaction, which contributes to covalent bonding in these complexes, becomes stronger going from Mn(II) to Co(II) (the σ contribution) and to Cu(II) (the π contribution). This change in the covalency results from the increased effective nuclear charge of the metal atom in going from Mn(II) to Zn(II) and the change in the 3d orbital populations (d^5→d^{10}). Ionic bonding also plays an important role in determining the overall strength of the ML$^+$–SC$_6$F$_5^-$ interaction. However, there is a compensating effect: as the covalent contribution to the metal–ligand bonding increases, the ionic contribution decreases. These results provide insight into the Irving–Williams series, where it is found that the bonding of the ligand being replaced by the thiolate makes a major contribution to the observed order of the stability constants over the series of metal ions.

1. Introduction

Blue copper centers, a critical component in biological electron transfer, represent some of the most well characterized active sites in the metalloproteins.[1] The geometry of the Cu site is trigonally distorted tetrahedral with three equatorial ligands, including two Cu−N(His) bonds at 2.0 Å, a short Cu−S(Cys) bond at 2.1 Å, and an axial S(Met) ligand with a long Cu−S bond at ~2.8 Å. The unique spectral features of the blue copper center include an intense low-energy charge-transfer band at 16700 cm^{-1} ($\epsilon \approx 5000$ M^{-1} cm^{-1}) in the absorption and a 2-fold reduced parallel hyperfine coupling relative to that of normal copper centers. These spectral features are the result of a highly covalent Cu−thiolate bond which facilitates long-distance electron transfer.[1−3] Many metal-substituted blue copper centers, which further probe the nature of the metal−thiolate interaction, have been made in the protein active sites.[4−13] Ad-

* To whom correspondence should be addressed. Fax: (650) 725-0259. E-mail: Edward.Solomon@Stanford.edu.
† Department of Chemistry, Stanford University.
‡ Stanford Synchrotron Radiation Laboratory, Stanford Linear Accelerator Center, Stanford University.
§ Department of Chemistry, University of Tsukuba.

(1) Solomon, E. I.; Szilagyi, R. K.; George, S. D.; Basumallick, L. *Chem. Rev.* **2004**, *104*, 419.
(2) Gewirth, A. A.; Cohen, S. L.; Schugar, H. J.; Solomon, E. I. *Inorg. Chem.* **1987**, *26*, 1133.
(3) Gewirth, A. A.; Solomon, E. I. *J. Am. Chem. Soc.* **1988**, *110*, 3811.
(4) McMillin, D. R.; Rosenberg, R. C.; Gray, H. B. *Proc. Natl. Acad. Sci. U.S.A.* **1974**, *71*, 4760.
(5) Tennent, D. L.; McMillin, D. R. *J. Am. Chem. Soc.* **1979**, *101*, 2307.
(6) Nar, H.; Huber, R.; Messerschmidt, A.; Filippou, A. C.; Barth, M.; Jaquinod, M.; van de Kamp, M.; Canters, G. W. *Eur. J. Biochem.* **1992**, *205*, 1123.
(7) Di Bilio, A. J.; Chang, T. K.; Malmström, B. G.; Gray, H. B.; Karlsson, B. G.; Nordling, M.; Pascher, T.; Lundberg, L. G. *Inorg. Chim. Acta* **1992**, *198−200*, 145.
(8) Bonander, N.; Vänngård, T.; Tsai, L.-C.; Langer, V.; Nar, H.; Sjölin, L. *Proteins: Struct., Funct., Genet.* **1997**, *27*, 385.
(9) Moratal, J. M.; Romero, A.; Salgado, J.; Perales-Alarcon, A.; Jimenez, H. R. *Eur. J. Biochem.* **1995**, *228*, 653.
(10) Chen, Z.-W.; Barber, M. J.; McIntire, W. S.; Mathews, F. S. *Acta Crystallogr.* **1998**, *D54*, 253.
(11) Funk, T.; Kennepohl, P.; Di Bilio, A. J.; Wehbi, W. A.; Young, A. T.; Friedrich, S.; Arenholz, E.; Gray, H. B.; Cramer, S. P. *J. Am. Chem. Soc.* **2004**, *126*, 5859.

ditionally, they provide insight into the specific assignments of the spectral features of the blue copper sites.

Recently, a series of metal-varied model complexes, [ML-(SC$_6$F$_5$)] (where L = HB(3,5-^{i}Pr$_2$pz)$_3^-$ and M^{2+} = Mn, Fe, Co, Ni, Cu, and Zn), related to the blue copper sites in proteins, has been synthesized and crystallographically characterized.[14,15] The metal atoms in [ML(SC$_6$F$_5$)] have a distorted tetrahedral coordination sphere with one M−S bond, two short equatorial M−N bonds, and an elongated axial M−N bond. The absorption features of these complexes are similar to those of the corresponding metal-substituted sites in the proteins, and the complexes show interesting systematic changes in the metal−thiolate bond lengths. The M−S bond length changes in the following order, which follows the Irving−Williams series for the stability constants: Mn(II) > Fe(II) > Co(II) > Ni(II) > Cu(II) < Zn(II).[16−18] Thus, these model complexes provide a systematic way to explore the different contributions to metal−thiolate bonding.

In this study, the combination of absorption, magnetic circular dichroism (MCD), resonance Raman (rR), and S K-edge X-ray absorption spectroscopies coupled with density functional calculations has been used to characterize the electronic structure of these complexes. Absorption and MCD spectroscopies provide a method for distinguishing the ligand-field transitions from the charge-transfer transitions. This provides insights into covalent interactions at the metal center. S K-edge XAS provides an estimate of the sulfur contribution in the ground-state wave function and the relative effective nuclear charges (Z_{nuc}^{eff}) at the metal atoms. DFT calculations evaluate the trends in bond energies, force constants, and bond orders and correlate these to the nature of the bonding between the metal ion and the thiolate ligand. In particular, this study examines the origin of the properties of the metal−ligand bonds for first-row transition metal complexes, the relative contributions of different covalent and ionic interactions to bonding, and the manner in which they produce the Irving−Williams series.

2. Experimental Section

2.1. Samples. The [ML(SC$_6$F$_5$)] complexes (where M^{2+} = Mn, Fe, Co, Ni, Cu, and Zn and L = HB(3,5-^{i}Pr$_2$pz)$_3^-$) were synthesized as described.[15] All reagents were of the highest grade commercially available and were used without further purification. The crystal structures of these complexes have been reported previously.[15] Preparation and handling of these complexes were done under an argon atmosphere in a Schlenk line.

2.2. UV−Vis Electronic Absorption and Magnetic Circular Dichroism Spectroscopy. Room-temperature (in a cyclohexane solution) UV−vis absorption spectra were recorded with a JASCO V-570 spectrophotometer using a quartz cell (0.10 cm in path length) in the 200−1700 nm region. Low-temperature (∼10 K) absorption spectra were obtained using a computer-interfaced Cary-500 spectrophotometer modified to accommodate a Janis Research Super Vari-Temp cryogenic dewar mounted in the light path. Low-temperature MCD spectra were recorded using two Jasco spectropolarimeters. Each is equipped with a modified sample compartment to accommodate focusing optics and an Oxford Instruments SM4000−7T superconducting magnet/cryostat. This arrangement allows data collection at temperatures from 1.6 to 290 K and fields up to 7 T. A Jasco J810 spectropolarimeter operating with an S-20 photomultiplier tube was used to access the visible and UV spectral region. A Jasco J200 spectropolarimeter operating with a liquid nitrogen-cooled InSb detector was used for the near-IR region. The PMT detector requires magnetic shielding. Solid samples (mulls) for spectroscopy were prepared by grinding microcrystalline material into powders with a mortar and pestle and adding mulling agents, poly(dimethylsiloxane) (Aldrich) or Fluorolube (Wilmad). This mixture was uniformly spread between quartz disks (Haraeus-Amersil), loaded into copper MCD cells, and promptly frozen. Depolarization of the light by the MCD samples was monitored by their effect on the CD signal of nickel (+)-tartrate placed before and after the sample. In all cases, the depolarization was less than 5%. Simultaneous Gaussian fitting of the low-temperature absorption and MCD spectra was performed using the Peak-Fit program (Jandel).

2.3. Resonance Raman. Raman spectra were recorded using a Princeton Instruments liquid nitrogen-cooled back-illuminated CCD camera mounted on a Spex 1877 0.6 m triple spectrometer equipped with holographic grating blazed at 1200, 1800, or 2400 grooves mm^{-1}. Kr ion (Innova 90C−K) and Ar ion (Sabre-25/7) visible and UV laser lines were used as variable energy excitation sources. Powder samples were loaded into 2 mm EPR tubes and stored in liquid nitrogen. Spectra were obtained in a ∼135° backscattering geometry with 20−30 mW of incident power. Raman scattering resolution and accuracy are ∼2 cm^{-1}. Raman peak profile intensities were determined relative to the 995 cm^{-1} band of solid Na$_2$SO$_4$.

2.4. X-ray Absorption Measurements and Data Reduction. The S K-edge data were measured using the 54-pole wiggler beam line 6-2 in high magnetic field mode of 10 kG with a Ni-coated harmonic rejection mirror and a fully tuned Si(111) double-crystal monochromator under ring conditions of 3 GeV and 60−100 mA. Details of the optimization of this beam line for low-energy absorption studies and the experimental setup have been described previously.[19] S K-edge measurements were performed at ∼4 °C. The solid samples were ground finely under a dry Ar atmosphere in a glovebag and dispersed as thinly as possible on Mylar tape to minimize the possibility of self-absorption effects. The temperature was regulated using a cryostat which uses a cooled N$_2$ gas through a channel in the sample holder. The sulfur fluorescence data were measured using an ionization chamber as a detector.[20,21]

The S K-edge data presented here were averaged and processed as described in an earlier publication.[22] Energy calibration was achieved using the S K-edge spectra of Na$_2$S$_2$O$_3$·5H$_2$O run at intervals between sample scans. The maximum of the first transition

(12) Jimenez, H. R.; Salgado, J.; Moratal, J. M.; Morgenstern-Badarau, I. *Inorg. Chem.* **1996**, *35*, 2737.
(13) De Kerpel, J. O. A.; Pierloot, K.; Ryde, U. *J. Phys. Chem. B* **1999**, *103*, 8375.
(14) Kitajima, N.; Fujisawa, K.; Tanaka, M.; Moro-Oka, Y. *J. Am. Chem. Soc.* **1992**, *114*, 9232.
(15) Matsunaga, Y.; Fujisawa, K.; Ibi, N.; Miyashita, Y.; Okamoto, K. *Inorg. Chem.* **2005**, *44*, 325.
(16) Irving, H.; Williams, R. J. P. *Nature* **1948**, *162*, 746.
(17) Irving, H.; Williams, R. J. P. *J. Chem. Soc.* **1953**, 3192.
(18) Williams, R. J. P. *Discuss. Faraday Soc.* **1958**, *26*, 123.

(19) Hedman, B.; Frank, P.; Gheller, S. F.; Roe, A. L.; Newton, W. E.; Hodgson, K. O. *J. Am. Chem. Soc.* **1988**, *110*, 3798.
(20) Stern, E. A.; Heald, S. M. *Rev. Sci. Instrum.* **1979**, *50*, 1579.
(21) Lytle, F. W.; Greegor, R. B.; Sandstrom, D. R.; Marques, E. C.; Wong, J.; Spiro, C. L.; Huffman, G. P.; Huggins, F. E. *Nucl. Instrum. Methods* **1984**, *226*, 542.
(22) Rose, K.; Shadle, S. E.; Glaser, T.; de Vries, S.; Cherepanov, A.; Canters, G. W.; Hedman, B.; Hodgson, K. O.; Solomon, E. I. *J. Am. Chem. Soc.* **1999**, *121*, 2353.

was assigned to 2472.02 eV. A smooth polynomial background of order 2 was fit to the pre-edge and subtracted from the entire spectrum. Normalization was achieved by fitting a linear polynomial to the post-edge and normalizing the edge jump to 1 at 2540 eV.[23] The area under the pre-edge peak was quantified by fitting the data using the program EDG-FIT.[24] The pre-edge and rising edge features were modeled with pseudo-Voigt line shapes with a fixed 1:1 Lorentzian/Gaussian ratio. The reported intensity and half-width value are based on an average over similar fits that accurately modeled the data and their second derivatives. In addition to the error resulting from the background correction and fitting procedure (ca. 2%), normalization procedures can introduce error (ca. 3%) in the total pre-edge peak areas.

2.5. Computational Details. Density functional theory (DFT) spin-unrestricted calculations were performed using the Gaussian 03 program (revision C.01).[25] Optimized geometries were calculated using the BP86[26,27] and B3LYP[28] exchange-correlation functionals with the triple-ζ 6-311+G(d) basis set.

The B3LYP functional with the triple-ζ 6-311+G(d) basis set was found to reproduce the crystal structure of the model complexes at an acceptable computational cost and was used for further calculations. Total energies were obtained by single-point calculations on these structures again using the B3LYP method but with the larger 6-311+G(3df) basis set. This improvement of the basis set did not change the energies by more than 2 kcal mol^{-1}. Tight SCF convergence criteria (10^{-8} a.u.) were used for all calculations. The complexes were modeled without isopropyl groups on the pyrazole ligands; their retention was found to have no substantial effect on the geometric or electronic structure. In addition, C_s symmetry was retained with a mirror plane containing the metal and axial pyrazole. Frequency calculations were performed to ensure that the stationary points were minima and to calculate infrared (IR) spectra. Calculated IR frequencies and intensities were transformed, via the SWizard program,[29] into simulated IR spectra using Lorentzian functions with half-widths of 15 cm^{-1}. High-spin electron configurations were used on the basis of the experimental data,[15] and wave function stability calculations were performed (using the *stable* keyword in Gaussian 03) to confirm that, in each case, the calculated wave function corresponded to the ground state.

The interaction energy, E_o, between the metal-pyrazolyl fragment (in the high-spin state) and the ligand X has been calculated as the energy of the interaction

$$ML^+ + X^- = [ML(X)]$$
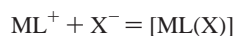
where $X = SC_6F_5$ and F (the fluoride is included for comparison to the thiolate in the discussion of the Irving−Williams series, section 5.4). The counterpoise correction[30] has been evaluated to account for the basis set superposition error (BSSE), and its magnitude was very small (<1 kcal mol^{-1}) in the B3LYP/6-311+G-(3df) calculations.

The bonding energy is partitioned into several contributions. First, E_o is separated into two components E_{prep} and E_{int}

$$E_o = E_{int} + E_{prep}$$

E_{prep} is the preparation (deformation) energy[31] necessary to transform the ML^+ and X^- fragments from their equilibrium geometries and electronic ground states to the those in the complexes

$$E_{prep} = E_{prep}(ML^+) + E_{prep}(X^-)$$

In this series, $E_{prep}(ML^+)$ and $E_{prep}(SC_6F_5^-)$ is 5.3−10.3 kcal mol^{-1} and 1.0−1.2 kcal mol^{-1}, respectively ($E_{prep}(F^-)$ is 0 kcal mol^{-1}). E_{int} is the interaction energy between the ML^+ and X^- fragments. This interaction energy can be further divided into two major components which can be interpreted in a physically meaningful way

$$E_{int} = E_{cov} + E_{ionic}$$

Here, E_{cov} is the covalent or orbital interaction energy (including the exchange repulsion energy[32−34]), and E_{ionic} is the electrostatic interaction energy. The latter is estimated to be a sum of the electrostatic interactions between charges, q^{NPA}, of atoms from the two molecular fragments, ML^+ and X^-

$$E_{ionic} = \sum_{a \in ML} \sum_{b \in X} \frac{q_a^{NPA} q_b^{NPA}}{r_{ab}} \text{ (in atomic units)}$$

The charge distribution in this calculation corresponds to the one in the complex, as opposed to the electrostatic interaction energy from the energy decomposition analysis of Kitaura−Morokuma[32,33,35] and Ziegler[36] which is calculated with *undistorted* charge distributions corresponding to those in the isolated fragments. Because the metal-pyrazolyl fragment and the X ligand carry opposite charges, the electrostatic interaction is attractive (E_{ionic} < 0) in the [ML(X)] complexes.

Molecular orbital (MO) compositions and the overlap populations between molecular fragments were calculated using the AOMix program.[37,38] Atomic charges and spin densities were calculated using the Mulliken[39−42] and natural[43] population analysis methods

(23) Ellis, P. J.; Freeman, H. C. *J. Synchrotron Radiat.* **1995**, *2*, 190.
(24) George, G. N. *EDG_FIT*; Stanford Synchrotron Radiation Laboratory, Stanford Linear Accelerator Center, Stanford University: Stanford, CA, 2000.
(25) Frisch, M. J.; Trucks, G. W.; Schlegel, H. B.; Scuseria, G. E.; Robb, M. A.; Cheeseman, J. R.; Montgomery, J. A., Jr.; Vreven, T.; Kudin, K. N.; Burant, J. C.; Millam, J. M.; Lyengar, S. S.; Tomasi, J.; Barone, V.; Mennucci, B.; Cossi, M.; Scalmani, G.; Rega, N.; Petersson, G. A.; Nakatsuji, H.; Hada, M.; Ehara, M.; Toyota, K.; Fukuda, R.; Hasegawa, J.; Ishida, M.; Nakajima, T.; Honda, Y.; Kitao, O.; Nakai, H.; Klene, M.; Li, X.; Knox, J. E.; Hratchian, H. P.; Cross, J. B.; Adamo, C.; Jaramillo, J.; Gomperts, R.; Stratmann, R. E.; Yazyev, O.; Austin, A. J.; Cammi, R.; Pomelli, C.; Ochterski, J. W.; Ayala, P. Y.; Morokuma, K.; Voth, G. A.; Salvador, P.; Dannenberg, J. J.; Zakrzewski, V. G.; Dapprich, S.; Daniels, A. D.; Strain, M. C.; Farkas, O.; Malick, D. K.; Rabuck, A. D.; Raghavachari, K.; Foresman, J. B.; Ortiz, J. V.; Cui, Q.; Baboul, A. G.; Clifford, S.; Cioslowski, J.; Stefanov, B. B.; Liu, G.; Liashenko, A.; Piskorz, P.; Komaromi, I.; Martin, R. L.; Fox, D. J.; Keith, T.; Al-Laham, M. A.; Peng, C. Y.; Nanayakkara, A.; Challacombe, M.; Gill, P. M. W.; Johnson, B.; Chen, W.; Wong, M. W.; Gonzalez, C.; Pople, J. A. *Gaussian 03*, revision C.01; Gaussian, Inc.: Wallingford, CT, 2004.
(26) Perdew, J. P. *Phys. Rev. B* **1986**, *33*, 8822.
(27) Becke, A. D. *Phys. Rev. A* **1988**, *38*, 3098.
(28) Becke, A. D. *J. Chem. Phys.* **1993**, *98*, 5648.
(29) Gorelsky, S. I. *SWizard*; Department of Chemistry, York University: Toronto, ON, 1999; http://www.sg-chem.net.
(30) Boys, S. F.; Bernardi, F. *Mol. Phys.* **1970**, *19*, 553.
(31) Bickelhaupt, F. M.; Baerends, E. J. *Rev. Comput. Chem.* **2000**, *15*, 1.
(32) Morokuma, K. *J. Chem. Phys.* **1971**, *55*, 1236.
(33) Kitaura, K.; Morokuma, K. *Int. J. Quantum Chem.* **1976**, *10*, 325.
(34) Chen, W.; Gordon, M. S. *J. Phys. Chem.* **1996**, *100*, 14316.
(35) Umeyama, H.; Morokuma, K. *J. Am. Chem. Soc.* **1977**, *99*, 1316.
(36) Ziegler, T.; Rauk, A. *Theor. Chim. Acta* **1977**, *46*, 1.
(37) Gorelsky, S. I., *AOMix*; Department of Chemistry, York University: Toronto, ON, 1997; http://www.sg-chem.net.
(38) Gorelsky, S. I.; Lever, A. B. P. *J. Organomet. Chem.* **2001**, *635*, 187.
(39) Mulliken, R. S. *J. Chem. Phys.* **1955**, *23*, 1833.
(40) Mulliken, R. S. *J. Chem. Phys.* **1955**, *23*, 1841.
(41) Mulliken, R. S. *J. Chem. Phys.* **1955**, *23*, 2338.
(42) Mulliken, R. S. *J. Chem. Phys.* **1955**, *23*, 2343.
(43) Reed, A. E.; Weinstock, R. B.; Weinhold, F. *J. Chem. Phys.* **1985**, *83*, 735.

(MPA and NPA, respectively), as implemented in Gaussian 03, and the Löwdin population analysis (LPA),[44] as implemented in AOMix-L.[37] The analysis of the MO compositions in terms of fragment molecular orbitals, construction of orbital interaction diagrams, and the charge decomposition analysis[45,46] was performed using AOMix-CDA.[37] Single-point B3LYP calculations with the TZVP basis set[47] for all atoms were used for molecular orbital analysis.

The Mayer bond orders,[48−51] $\mathbf{B}_{AB}$, were obtained using AOMix-L to analyze the chemical bonding between molecular fragments A and B

$$\mathbf{B}_{AB} = \sum_{a \in A} \sum_{b \in B} [(\mathbf{PS})_{ba}(\mathbf{PS})_{ab} + (\mathbf{P^s S})_{ba}(\mathbf{P^s S})_{ab}] = \mathbf{B}_{AB}{}^{\alpha} + \mathbf{B}_{AB}{}^{\beta}$$

$$\mathbf{B}_{AB}{}^{\alpha} = 2 \sum_{a \in A} \sum_{b \in B} (\mathbf{P^{\alpha} S})_{ba}(\mathbf{P^{\alpha} S})_{ab}$$

$$\mathbf{B}_{AB}{}^{\beta} = 2 \sum_{a \in A} \sum_{b \in B} (\mathbf{P^{\beta} S})_{ba}(\mathbf{P^{\beta} S})_{ab}$$

where $\mathbf{P}$ and $\mathbf{P^s}$ are the density and spin-density matrices, respectively ($\mathbf{P} = \mathbf{P^{\alpha}} + \mathbf{P^{\beta}}$ and $\mathbf{P^s} = \mathbf{P^{\alpha}} - \mathbf{P^{\beta}}$), $\mathbf{P^{\alpha}}$ and $\mathbf{P^{\beta}}$ are α- and β-electron density matrices, and $\mathbf{S}$ is the overlap matrix. The symmetry-adapted combinations of basis functions were used to allow a decomposition of the bond orders according to irreducible representations of the C_s point group

$$\mathbf{B}_{AB} = \sum_{\Gamma} \mathbf{B}_{AB}(\Gamma)$$

This analysis delivers local information on the chemical bonding between molecular fragments, and the symmetry decomposition enables one to find the σ- and π-contributions to bond orders.

Force constants were calculated by fitting the metal-pyrazolyl fragment−X ligand potential surface to the polynomial function

$$E = E_0 + {}^1/_2 k(d - d_0)^2 + k_a(d - d_0)^3$$

Time-dependent density functional theory (TDDFT)[52,53] was used to calculate the energies and intensities of the 60 lowest-energy electronic transitions of each model complex. These were transformed, using the SWizard program,[29] into simulated spectra as described before,[54] using Gaussian functions with half-widths of 2500 cm^{-1}.

3. Results

3.1. Electronic Absorption and Magnetic Circular Dichroism.
Figure 1 presents the room-temperature solution absorption and low-temperature mull MCD spectra of [NiL-(SC$_6$F$_5$)], [CoL(SC$_6$F$_5$)], and [FeL(SC$_6$F$_5$)]. Gaussian resolution (depicted as dashed lines in the spectra) of the absorption

(44) Löwdin, P.-O. *Adv. Quantum Phys.* **1970**, *5*, 185.
(45) Dapprich, S.; Frenking, G. *J. Phys. Chem.* **1995**, *99*, 9352.
(46) Gorelsky, S. I.; Solomon, E. I. To be published.
(47) Schafer, A.; Huber, C.; Ahlrichs, R. *J. Chem. Phys.* **1994**, *100*, 5829.
(48) Mayer, I. *Chem. Phys. Lett.* **1983**, *97*, 270.
(49) Mayer, I. *Theor. Chim. Acta* **1985**, *67*, 315.
(50) Mayer, I. *Int. J. Quantum Chem.* **1986**, *29*, 73.
(51) Mayer, I. *Int. J. Quantum Chem.* **1986**, *29*, 477.
(52) Casida, M. E. In *Recent Advances in Density Functional Methods*; Chong, D. P., Ed.; World Scientific: Singapore, 1995; p 155.
(53) Stratmann, R. E.; Scuseria, G. E.; Frisch, M. J. *J. Chem. Phys.* **1998**, *109*, 8218.
(54) Gorelsky, S. I. In *Comprehensive Coordination Chemistry-II*; Mc-Cleverty, J. A., Meyer, T. J., Eds.; Elsevier: Amsterdam, 2004; Vol. 2, p 467.

Figure 1. Absorption and MCD spectra of (A) [NiL(SC$_6$F$_5$)], (B) [CoL-(SC$_6$F$_5$)], and (C) [FeL(SC$_6$F$_5$)]. Room-temperature absorption and low-temperature MCD at 5 K and 7 T. Gaussian fits overlaid.

spectra was obtained from a simultaneous fit of the absorption and MCD spectra for each of the complexes. Transitions gain MCD intensity by spin−orbit coupling. Thus, the ligand-field (LF) transitions have a higher MCD intensity than the charge-transfer (CT) transitions, which involve S or N character, because the spin−orbit coupling parameter for the metal is greater than for S and N: $\xi(Cu^{2+}) = 830$ cm^{-1}, $\xi(Ni^{2+}) = 630$ cm^{-1}, $\xi(Co^{2+}) = 515$ cm^{-1}, $\xi(Fe^{2+}) = 400$ cm^{-1}, $\xi(S) = 382$ cm^{-1}, and $\xi(N) = 70$ cm^{-1}.[55] MCD transitions also have a sign which facilitates band resolution and assignment. On the other hand, absorption intensity is high for charge-transfer (CT) transitions with large orbital overlaps.

The bands observed for each of the complexes can be differentiated as LF and CT transitions by their relative intensities in absorption and MCD spectra. The ratio of MCD-to-absorption intensity approximates the C_0/D_0 ratio for the mulls (C_0 is the MCD C-term intensity, and D_0 is the dipole strength in absorption).

In the high-energy ($>15\,000$ cm^{-1}) region, the absorption spectrum (Figure 1A) of [NiL(SC$_6$F$_5$)] is dominated by intense absorptions at 30000 cm^{-1} (1120 M^{-1} cm^{-1}), 28 000 cm^{-1} (1700 M^{-1} cm^{-1}), 23 200 cm^{-1} (3060 M^{-1} cm^{-1}), and 20 100 cm^{-1} (875 M^{-1} cm^{-1}). The low MCD/absorption

(55) (a) These are free-ion values. Covalent reduction of these (because of the relativistic nephelauxetic effect) is small. (b) Neese, F.; Solomon, E. I. *Inorg. Chem.* **1998**, *37*, 6568.

ratios and the rR enhancements (vide infra) of these bands clearly indicate that they are the result of CT transitions. In the lower-energy region, there are weak absorption bands (ϵ < 100 M^{-1} cm^{-1}) at 12 500 and 6250 cm^{-1}. On the basis of their high MCD/absorption ratios these are assigned as LF transitions. Tetrahedral Ni(II) complexes show a visible band at ∼14 000 cm^{-1} with multiplet structures from the spin-allowed $^3T_1(F) \rightarrow ^3T_1(P)$ transition. They also exhibit additional spin-allowed transitions at lower energies (∼8000 and 5000 cm^{-1}) because of the $^3T_1(F) \rightarrow ^3A_2(F)$ and $^3T_1(F) \rightarrow ^3T_2(F)$ transitions. Hence, in [NiL(SC$_6$F$_5$)] the 12 500 cm^{-1} band is assigned to the $^3T_1(F) \rightarrow ^3T_1(P)$ transition (pseudo A because of the in-state spin−orbit coupling); the 9500 cm^{-1} band (observed in MCD) is assigned to the $^3T_1(F) \rightarrow ^3A_2(F)$ transition, and the 6250 cm^{-1} band is assigned to the $^3T_1(F) \rightarrow ^3T_2(F)$ transition.

The [CoL(SC$_6$F$_5$)] complex exhibits intense absorption (Figure 1B) at 32 000 cm^{-1} (4900 M^{-1} cm^{-1}), 29 400 cm^{-1} (2000 M^{-1} cm^{-1}), and 28 000 cm^{-1} (1300 M^{-1} cm^{-1}). Again, these high-energy bands are assigned to CT transitions on the basis of their low MCD/absorption (C_0/D_0) ratios. The lower-energy (<22 000 cm^{-1}) bands at 16 500, 12 000, and 7000 cm^{-1} are relatively more intense in the MCD spectrum as compared to the bands in the absorption spectrum, which indicates that they are associated with LF transitions. Four-coordinate Co(II) complexes typically have an absorption band at ∼15 000 cm^{-1} which is assigned to the $^4A_2 \rightarrow ^4T_1$-(P) transition.[56] The fine structure observed for this absorption band is attributed to spin−orbit coupling within the T_1 state (providing the pseudo-A feature in MCD). The other bands observed in the visible and near-IR region are assigned to the $^4A_2 \rightarrow ^4T_1(F)$ at ∼12 500 cm^{-1} and the $^4A_2 \rightarrow ^4T_2(F)$ at 7000 cm^{-1} spin-allowed transitions.

Figure 1C presents the absorption and MCD spectra for [FeL(SC$_6$F$_5$)]. This complex exhibits intense absorption at 32 500 cm^{-1} (5850 M^{-1} cm^{-1}) and 28 000 cm^{-1} (1390 M^{-1} cm^{-1}), and weak absorption at 7000 cm^{-1} (<100 M^{-1} cm^{-1}). (Note that the MCD spectrum was collected using two spectrophotometers, one covering the range from 5000 to 16 000 cm^{-1} and the second the range of 13 000−33 000 cm^{-1}, where the overlap region 13 000−16 000 cm^{-1} is used to scale the two individual spectra for the mull sample. Because of the absence of any spectral feature in the overlap region for the ferrous complex, the data in the two spectral regions could not be scaled accurately.) The MCD investigations of four-coordinate iron model complexes have shown that distorted tetrahedral sites exhibit two LF transitions in the 4000−7000 cm^{-1} region. The observed MCD spectral pattern (two bands in 5000−7000 cm^{-1} region) in the Fe complex is analogously assigned to LF transitions. The other higher-energy bands (which are orders of magnitude more intense in absorbance than LF transitions but comparable in MCD intensity) are assigned to CT transitions.

Figure 2 compares the electronic absorption spectra (5000−33 000 cm^{-1}) of the [ML(SC$_6$F$_5$)] complexes. Zn (d^{10})

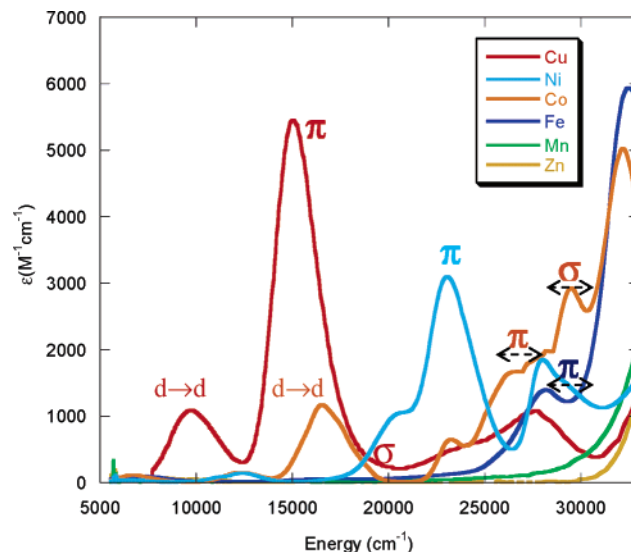**Figure 2.** UV−vis absorption spectra of [ML(SC$_6$F$_5$)] in cyclohexane at room temperature.

and Mn (d^5) do not show significant absorption in the visible region (the former has a filled shell and the latter has only spin-forbidden LF transitions and CT transitions to high energy). The absorption spectrum of the copper complex matches those of a similar complex, [CuL(SCPh$_3$)],[57] the primary feature being the intense CT band associated with the ligand-to-metal S(thiolate) p$\pi \rightarrow$ Cu d$_{x^2-y^2}$ (LMCT) transition. The LF transitions are to lower energy. Because of the presence of the SC$_6$F$_5$ thiolate, there are additional absorption bands in the 23 000−30 000 cm^{-1} region (Figure 2) when compared to the spectrum of the [CuL(SCPh$_3$)] complex.

Similar to [CuL(SC$_6$F$_5$)], the Ni complex also exhibits an intense S(thiolate) p$\pi \rightarrow$ Ni d$_{x^2-y^2}$ CT transition. This transition is shifted to higher energy and decreased in intensity relative to the Cu complex. In going from Ni to Co, the S(thiolate) p$\pi \rightarrow$ M d$_{x^2-y^2}$ transition shifts to still higher energy and further decreases in intensity. Importantly, a new feature at higher energy and with increased intensity, relative to the S(thiolate) p$\pi \rightarrow$ Co d$_{x^2-y^2}$ LMCT transition, is present in the Co complex. This band is assigned to the S(thiolate) p$\sigma \rightarrow$ Co d$_{xy}$ LMCT transition. Further, the Fe complex also exhibits an intense higher-energy CT transition above 30 000 cm^{-1}, which could be assigned to the S(thiolate) p$\sigma \rightarrow$ Fe transition. Thus, the interesting trends observed are as follows: (1) upon going from Cu $\rightarrow$ Ni $\rightarrow$ Co, the S(thiolate) p$\pi \rightarrow$ M d$_{x^2-y^2}$ transition shifts to higher energy and decreases in intensity and (2) a new S(thiolate) p$\sigma \rightarrow$ M d$_{xy}$ band appears upon going from Ni to Co, which shifts to higher energy in going from Co to Fe.

3.2. Resonance Raman Spectroscopy. The resonance Raman (rR) spectra for [ML(SC$_6$F$_5$)] (M= Cu, Ni, and Co) are characterized by a dominant strong peak at 400−411 cm^{-1}, which is associated with M−S stretching (Figure 3). This band is resonance enhanced through the S(thiolate) p$\pi \rightarrow$ M d$_{x^2-y^2}$ CT transition. There are also additional weak

(56) Lever, A. B. P. *Inorganic Electronic Spectroscopy*, 2 ed.; Elsevier: Amsterdam, 1984.

(57) Randall, D. W.; DeBeer George, S.; Hedman, B.; Hodgson, K. O.; Fujisawa, K.; Solomon, E. I. *J. Am. Chem. Soc.* **2000**, *122*, 11620.
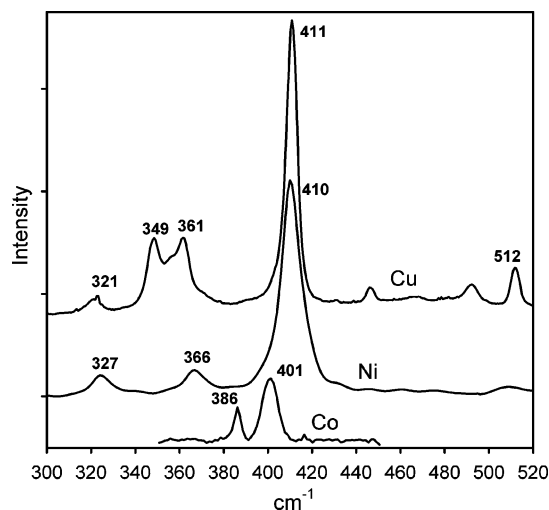
Figure 3. Resonance Raman spectra of [ML(SC₆F₅)], M= Cu (excitation wavelength λ_o = 676 nm), Ni (λ_o = 458 nm), and Co (λ_o = 407 nm).

bands in the 300−500 cm^{-1} region. These weaker bands have been attributed to kinematic coupling of the M−S stretching with other vibrational modes of [ML(SC₆F₅)]. The rR spectrum of the [CuL(SC₆F₅)] complex resembles those of the [CuL(SCPh₃)] complex, studied previously.[57] In the latter, however, the Cu−S vibrational frequency (421 cm^{-1}) is greater than that of [CuL(SC₆F₅)] (411 cm^{-1}) indicating that the Cu−S force constant in [CuL(SC₆F₅)] is somewhat weaker than in the complex with the more electron-rich SCPh₃ thiolate but similar to the Cu−S force constants in typical blue copper proteins.[1]

The intensity-weighted average frequency,[58] $\langle\nu_{M-S(thiolate)}\rangle$, of the 400 cm^{-1} envelope for the [ML(SC₆F₅)] complexes does not show large variation. This agrees with the observation that the experimental[15] and calculated (Figure S1 in Supporting Information) IR spectra of these complexes in the 300−500 cm^{-1} region are very similar.

The Fe−S stretching vibration has not been detected in the rR spectrum by using the excitation in the absorption bands of [FeL(SC₆F₅)] in the 23 000−30 000 cm^{-1} spectral region. Instead, very strong resonances at 1410 and 1675 cm^{-1} were observed (Figure S2 in Supporting Information). These two bands are also present in the spectra of the other complexes, when the Raman excitation energy is in the 23 000−30 000 cm^{-1} region. The high frequencies of these vibrations are consistent with intraligand aromatic C−C and C−N stretches. This type of geometric distortion would be expected for an excited electronic state with a π-antibonding interaction between atoms in the aryl thiolate ligand. Because the 1410 and 1675 cm^{-1} bands are observed for all of the complexes and their energies are independent of the metal atom, they can be assigned to the SC₆F₅ thiolate vibrational bands. DFT calculations of the vibrational spectra of the complexes support this assignment (vide infra). Thus, the absorption spectra in the near-UV region all have significant contributions from thiolate intraligand electronic transitions.

Figure 4. (A) Normalized S K-edge XAS spectra of [M−S(C₆F₅)] complexes (M = Mn(II), green line; Fe(II), dark blue line; Co(II), orange line; Ni(II), light blue line; Cu(II), red line; and Zn(II), brown line). (B) The 2nd derivative spectra showing the shift in the 1s→ ψ^* transition as well as the edge transition between 2471.5 and 2473.0 eV. The circles and solid rectangles indicate the pre-edge peak maxima and the edge transition, respectively.

3.3. XAS Sulfur K Edges. The S K-edge spectra of the [ML(SC₆F₅)] series are shown in Figure 4. A low-energy pre-edge feature is observed in the 2469−2472 eV range. The energy position varies in the following order: Cu(II) < Ni(II) < Co(II) < Fe(II). The pre-edge feature for the Fe and Mn complexes is shifted into the edge but is observed in the second derivative spectrum for [FeL(SC₆F₅)]. The Zn complex, which has a filled d manifold, lacks this transition. This transition is assigned as a ligand 1s → ψ^* transition, and in the case of a d⁹ system, ψ^* is the singly occupied HOMO.[59,60] Because of the localized nature of the S 1s orbital, this transition can gain intensity only if there is a significant component of the S 3p character mixed in the ψ^* orbital; thus, the observed pre-edge transition intensity is the intensity of the pure dipole-allowed 1s → 3p transition weighted by α^2 (M 3d−S 3p covalency of the bond)

$$\psi^* = (1 - \alpha^2 - \beta^2)^{1/2}|M\ 3d\rangle - \alpha|S\ 3p\rangle - \beta\ |other\ L\rangle$$

$$I(S\ 1s \rightarrow \psi^*) = \alpha^2 I(S\ 1s \rightarrow S\ 3p)$$

Integrating the area under the pre-edge peak thus provides a direct probe of the M 3d−S(thiolate) covalency.[61] Quanti-

(58) Blair, D. F.; Campbell, G. W.; Schoonover, J. R.; Chan, S. I.; Gray, H. B.; Malmström, B. G.; Pecht, I.; Swanson, B. I.; Woodruff, W. H.; Cho, W. K.; English, A. M.; Fry, H. A.; Lum, V.; Norton, K. A. *J. Am. Chem. Soc.* **1985**, *107*, 5755.
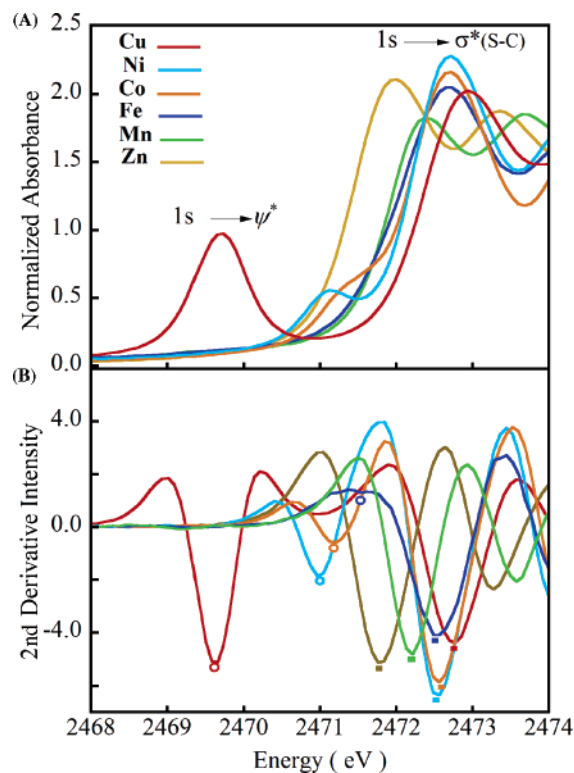
(59) Shadle, S. E.; Penner-Hahn, J. E.; Schugar, H. J.; Hedman, B.; Hodgson, K. O.; Solomon, E. I. *J. Am. Chem. Soc.* **1993**, *115*, 767.
(60) Shadle, S. E.; Hedman, B.; Hodgson, K. O.; Solomon, E. I. *J. Am. Chem. Soc.* **1995**, *117*, 2259.
(61) DeBeer George, S.; Metz, M.; Szilagyi, R. K.; Wang, H. X.; Cramer, S. P.; Lu, Y.; Tolman, W. B.; Hedman, B.; Hodgson, K. O.; Solomon, E. I. *J. Am. Chem. Soc.* **2001**, *123*, 5757.
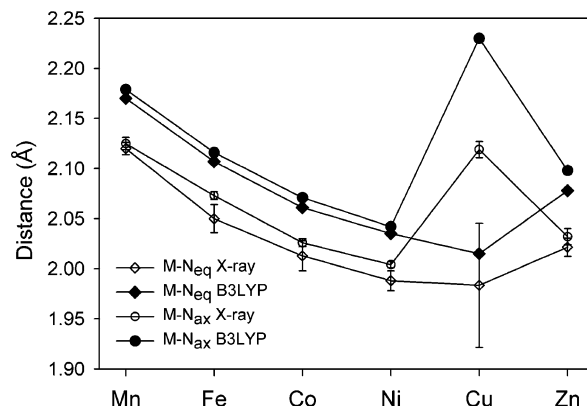
Table 1. Sulfur K-Edge XAS Results for the [ML(SC$_6$F$_5$)] Complexes

M	1s → ψ* pre-edge energy (eV)[a]	1s → σ*(S−C) transition energy (eV)[b]	% of S character in ψ*
Zn(II)	n/a	2471.8	−
Cu(II)	2469.7	2472.8	28
Ni(II)	2470.9	2472.6	6
Co(II)	2471.3	2472.6	5
Fe(II)	2471.4[c]	2472.5	−
Mn(II)	−	2472.2	−

[a] The estimated error is ± 0.1 eV. [b] Determined from the second derivative experimental spectra. [c] Error in energy estimation is higher as the pre-edge is barely resolvable in the second derivative spectrum.

tation of the S character in the ψ* for the Cu(II) and Ni(II) complexes gives 28% and 6% S 3p character (weighted by the number of d holes), respectively. This is in very good agreement with the DFT calculations (section 4.2). For both Co(II) and Fe(II), the parent excited states can mix with the higher-lying states (overlapping the edge) of appropriate symmetry, which derive from formally forbidden two-electron excitations.[60] This mixing redistributes some of the intensity predicted by the strong-field dipole strength (for the transition to the allowed d^{n+1} excited state) to higher-energy states overlapping the edge. The magnitude of this mixing can be estimated from the Tanabe-Sugano matrices assuming reasonable excited-state Dq and B values.[62,63] In the Co(II) complex, the excited-state mixing is estimated to be 16%. The parent excited state (pre-edge) accounts for ~4% of the S character in the ψ*, which indicates a M 3d−S 3p covalency of ~ 5%. In the case of the Fe(II) and Mn(II) complexes, the pre-edge is completely shifted into the edge, which makes the experimental estimation of covalency inaccessible.

The energy of the pre-edge transition is determined by the following three factors: the S atomic charge, the ligand field on the metal ion, and the Z_{nuc}^{eff} on the metal 3d manifold.[60,64] In contrast, the energy of the edge transition is determined by the S atomic charge. Thus, the pre-edge transition energy, corrected for the shift in the edge energy, will reflect the combined effect of the ligand field and Z_{nuc}^{eff} on the metal. In addition, because all of the complexes are tetrahedral with the same ligand set, the ligand-field effects in modulating the pre-edge transition energy are expected to be similar in the [ML(SC$_6$F$_5$)] series. Thus, the energy shifts of the edge and 1s → ψ* transitions, together, can determine the trend in the metal effective nuclear charge in [ML(SC$_6$F$_5$)] (M = Fe to Cu).

The intense electric dipole-allowed transition observed at the onset of the edge jump in the S K-edge spectra at ~2473 eV is the 1s → σ*(S−C) transition. This transition shifts to higher energy in the following order: Zn(II) < Mn(II) < Fe(II) < Co(II) = Ni(II) < Cu(II) (Figure 4, Table 1). This trend reflects a decrease in the negative charge on the sulfur atom as a result of covalent donation from the thiolate ligand to the metal 3d orbitals (section 4.2), as observed from the

(62) Karpishin, T. B.; Gebhard, M. S.; Solomon, E. I.; Raymond, K. N. *J. Am. Chem. Soc.* **1991**, *113*, 2977.
(63) Ferguson, J. *Prog. Inorg. Chem.* **1970**, *12*, 159.
(64) Shadle, S. E.; Hedman, B.; Hodgson, K. O.; Solomon, E. I. *Inorg. Chem.* **1994**, *33*, 4235.

Figure 5. Experimental[14,15] and calculated M−N bond lengths in the [ML-(SC$_6$F$_5$)] complexes.

pre-edge intensity (vide supra). Interestingly, both the edge-transition energy and the M 3d-thiolate covalency are similar for Ni(II)− and Co(II)−thiolate complexes. Co(II) has one more vacant orbital (d$_{xy}$) than Ni(II). This results in an additional σ covalent interaction in the Co(II) complex, which would decrease the negative charge on sulfur. However, the M 3d−S pπ covalency is weakened upon going from Ni(II) to Co(II) which results in similar edge energies and S 3p character mixed into the metal d orbitals. In the Zn(II) complex, the edge transition is 1 eV lower in energy than the Cu(II) complex indicating more electron density on S in the Zn(II) complex consistent with the less covalent M−S bond in the d^{10} configuration (section 4.4).

A comparison of the edge-corrected pre-edge energies (1s → ψ*), using the trend observed in the edge-transition (1s → σ*(S−C)) energy, furnishes the trend in Z_{nuc}^{eff} on the metal ion. The edge-corrected pre-edge energy increases upon changing from Cu(II) to Ni(II) to Co(II) to Fe(II) (Table 1). This transition is ~1.4 eV higher in energy for Ni(II) than for Cu(II), 0.4 eV higher for Ni(II) than for Co(II), and 0.2 eV higher for Co(II) than for Fe(II) in [ML(SC$_6$F$_5$)]. Because a greater Z_{nuc}^{eff} of the metal ion would decrease the energy of the metal 3d manifold leading to a decrease in the 1s → ψ* transition energy, the Z_{nuc}^{eff} is largest for Cu(II) in the series.

4. Analysis

4.1. Geometric Structure, M−S Bond Energies, Force Constants, and Bond Orders. The metal atom in [ML-(SC$_6$F$_5$)] has a distorted tetrahedral coordination sphere with two short equatorial M−N bonds and an elongated axial M−N bond (Figure 5; the metal−ligand distances and Cartesian atomic coordinates of the optimized structures are available in the Supporting Information). The Cu−N$_{ax}$ bond distance is especially long because of the Jahn−Teller distortion for the (e)^4(t$_2$)^5 electronic configuration.

While the M−N$_{eq}$ bond distances decrease monotonically from Mn to Cu, the M−S bond length decreases sharply from Mn to Fe, changes little from Fe(II) to Co(II) and Co(II) to Ni(II), decreases again from Ni(II) to Cu(II) and increase to Zn (Figure 6A). The M−L distances from the B3LYP/6-311+G(d) calculations are somewhat longer than those
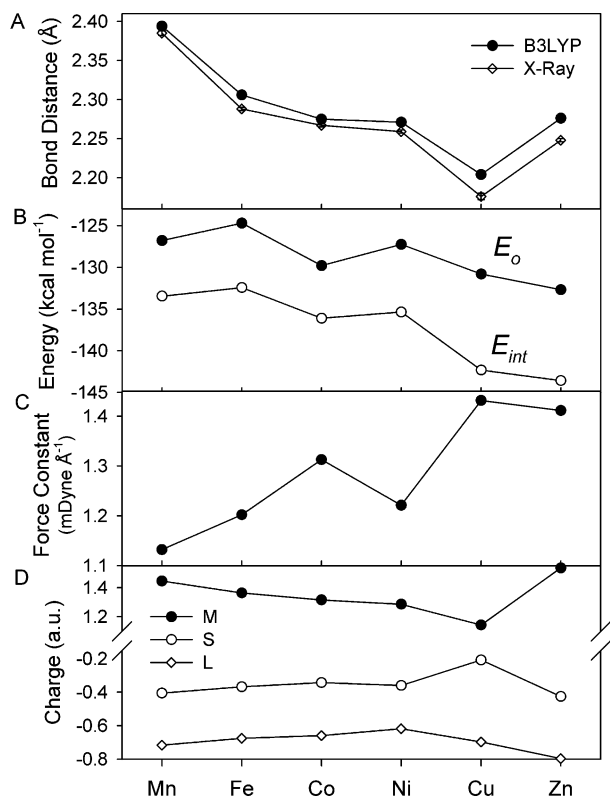
Figure 6. (A) Experimental and calculated M−S bond lengths in the [ML-(SC$_6$F$_5$)] complexes, (B) calculated binding energies, E_o, and interaction energies, E_{int}, between the ML$^+$ and SC$_6$F$_5$$^-$ fragments, (C) calculated M−S force constants, and (D) the NPA charges of the metal and sulfur atoms and the pyrazolyl ligand L.

determined crystallographically (the mean absolute deviation (MAD) is 0.048 and 0.017 Å for the M−N$_{eq}$ and M−S bond lengths, respectively). The difference between the calculated and experimental values for the Cu−N$_{ax}$ bond length is ∼0.1 Å, but it corresponds to the weakest Cu−N interaction and is easily influenced by other factors. The energy corresponding to the Cu−N$_{ax}$ bond length change from 2.23 to 2.12 Å (expr.)[14] is only 0.43 kcal mol^{-1}. Overall, the B3LYP calculations reproduce all experimentally observed structural changes very well. The BP86 functional also predicts the same trends in the M−S bond lengths as the B3LYP functional but, because of the overly covalent tendency of the BP86 functional,[1] the M−S distances from the BP86 calculations are consistently shorter (by 0.02−0.07 Å) than those from the B3LYP calculations and the X-ray structures.[14,15] The nonmonotonic variations in the M−S bond lengths (Figure 6) mark important changes in the metal−thiolate bonding, depending on the electronic configuration of the metal ion (vide infra).

Generally, it is expected that the shorter bond will be stronger. More rigorously, the bond strength should be described by two main parameters, the bonding energy (E_o) and the force constant, k. The latter represents the potential energy surface (PES) curvature near the minimum

$$k = \left(\frac{\partial^2 E}{\partial R_{M-S}^2} \right)_{R=R_o}$$

The calculated ML$^+$ − SC$_6$F$_5$$^-$ binding energy, E_o, in [ML-(SC$_6$F$_5$)] ranges (Figure 6B) from −124.7 kcal mol^{-1} for Fe to −132.7 kcal mol^{-1} for Zn, and its variation does not mirror the changes in the M−S bond lengths. The M−S force constant is lowest for the Mn complex (1.13 mDyne Å^{-1}), and it increases from Mn to Fe to Co, where it reaches a local maximum; then it decreases for the Ni complex, and increases for the Cu(II) complex (the maximum value is 1.43 mDyne Å^{-1}). It then decreases again for the Zn(II). The force constant (Figure 6C) shows greater variation (26%) than the bond energy (6%). Its variation is more consistent with the changes in the M−S bond lengths.

The chemical bonding in transition metal complexes is usually described in terms of ionic and covalent interactions between the metal and the ligands. In many transition metal complexes (especially complexes of first-row transition metals), the ionic contribution to metal−ligand bonding is thought to be dominant. However, in [ML(SC$_6$F$_5$)], the metal−thiolate bonding also has a significant covalent contribution. This is reflected in the experimental spectra (section 3) and the metal−thiolate orbital mixing, which will be discussed in section 4.2. The ionic contribution is related to the atomic charges of the metal and the sulfur of the thiolate ligand (Figure 6D). It can be seen that the absolute values of the metal and sulfur charges are highest in the Mn and Zn complexes and lowest in the Cu complex. All of the population analysis methods employed (MPA, LPA, and NPA) show this trend. Thus, the ionic contribution to the M−S bond energy is lowest in the Cu complex and highest in the Mn and Zn complexes.

4.2. Ground-State Electronic Structure. Figure 7 and Figures S3 and S4 (Supporting Information) show MO diagrams for the [ML(SC$_6$F$_5$)] complexes, with the metal 3d orbitals and the thiolate ligand orbitals labeled. Contour surfaces of the frontier molecular orbitals are presented in Figure 8. These MOs are relevant for chemical bonding between the metal atom and the thiolate ligand and define the optical spectra of the corresponding [ML(SC$_6$F$_5$)] complexes (section 4.3). The metal−ligand covalent interaction involves charge donation from the SC$_6$F$_5$$^-$ ligand to the ML$^+$ fragment (Table 2). From the charge decomposition analysis,[37,45] the *back-donation* from the ML$^+$ fragment to the thiolate ligand is very small in this series despite the less-electron donating character of the pentafluorinated thiolate ligand (for example, the orbital contribution of all of the α-spin-unoccupied SC$_6$F$_5$$^-$ fragment orbitals to all 119 α-spin-occupied MOs of the complexes is only 2.7−4.3% (Table 2), out of 11900%).

In the Mn complex, all of the β-spin 3d orbitals of the central atom are unoccupied. The β-spin HOMO of the complex is the S(thiolate) pπ orbital, which corresponds to the highest-occupied fragment orbital of SC$_6$F$_5$$^-$. The occupied S(thiolate) pσ orbital (HOMO-3, which corresponds to HOMO-1 of the SC$_6$F$_5$$^-$ fragment) is 1.4 eV lower in energy than the HOMO. These two thiolate-occupied fragment orbitals are the main contributors to the covalent bonding between the metal ion and the thiolate. The 119 α-spin-occupied and 114 β-spin-occupied MOs of the Mn
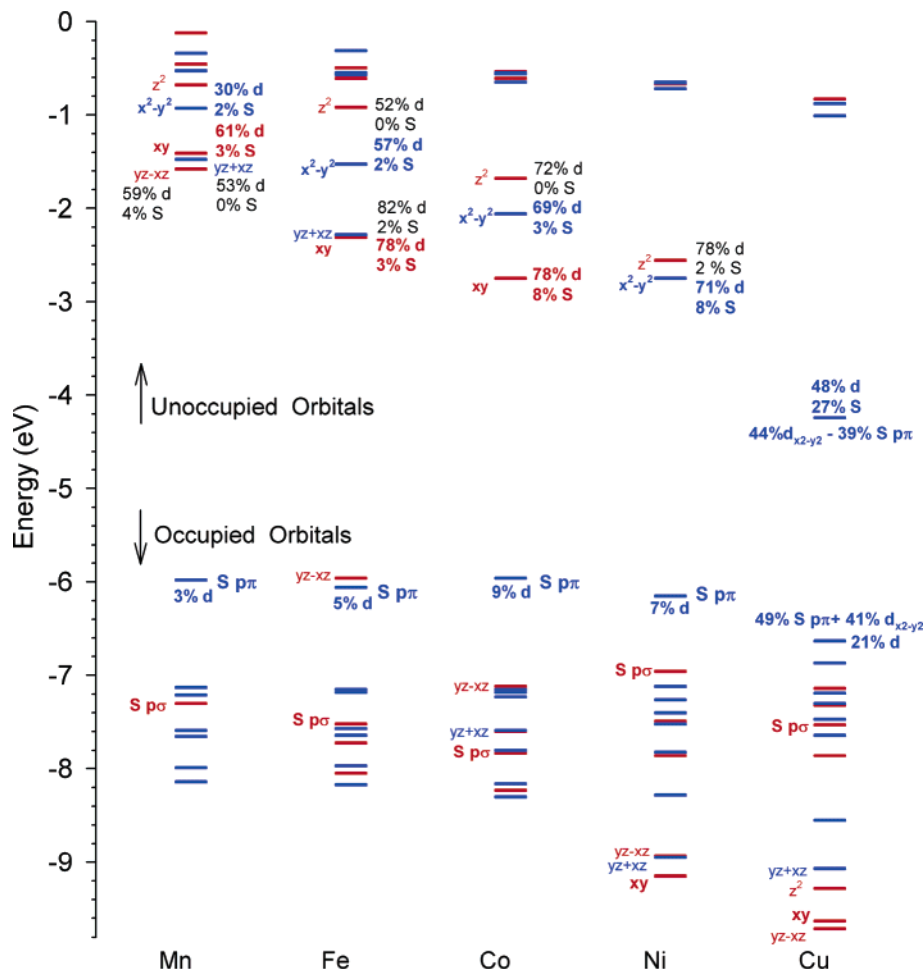
Figure 7. β-Spin frontier molecular orbitals of the [ML(SC$_6$F$_5$)] complexes (MOs with a' and a'' symmetry are shown in red and blue, respectively).

Table 2. Total Contributions (%) of Unoccupied Fragment Molecular Orbitals to the Occupied Orbitals of [ML(SC$_6$F$_5$)], the Resulting Charge Transfer (a.u.) from the SC$_6$F$_5^-$ Thiolate to the ML$^+$ Fragment, and the NPA Spin Density s^{NPA} (a.u.) on the Thiolate Ligand in the Complexes

	Mn	Fe	Co	Ni	Cu	Zn
donation (SC$_6$F$_5^- \rightarrow$ ML$^+$) and polarization (ML$^+$)[a]						
% (α-spin UFO of ML$^+$)	29.5	29.6	28.2	28.2	26.2	32.5
% (β-spin UFO of ML$^+$)	32.0	33.6	48.9	47.3	81.7	32.5
back-donation (SC$_6$F$_5^- \leftarrow$ ML$^+$) and polarization (SC$_6$F$_5^-$)						
% (α-spin UFO of SC$_6$F$_5^-$)	3.1	3.5	3.5	3.4	4.3	2.7
% (β-spin UFO of SC$_6$F$_5^-$)	2.7	4.8	4.2	3.7	4.0	2.7
Δq^{NPA} (SC$_6$F$_5^- \rightarrow$ ML$^+$)	0.32	0.36	0.38	0.37	0.57	0.28
s^{NPA}(SC$_6$F$_5^-$)	0.13	0.16	0.17	0.16	0.38	0.00

[a] Polarization of the ML$^+$ fragment reflects its charge distribution due to thiolate binding.

complex contain a total of 29.5% and 32% of the orbital character of the unoccupied molecular orbitals of the ML$^+$ fragment, respectively (Table 2).

Because the difference between the β- and α-spin-unoccupied fragment molecular orbital (ML$^+$) contributions (Table 2) is less than 3%, the Mn 3d−thiolate orbital interactions are weak and contribute little to the covalent bonding, relative to the stronger Mn 4s,4p−thiolate orbital interaction. This can be confirmed by looking at the composition of the frontier orbitals. The Mn 3d orbital characters of the thiolate-based HOMO(π) and HOMO-3(σ)

(the SC$_6$F$_5^-$ contributions are 95% and 86%, respectively) are 3% and 5%, respectively, and reciprocally, the S orbital contribution is 2% for the Mn d$_{x^2-y^2}$ (dπ) orbital and 3% for the d$_{xy}$ (dσ) orbital (Figure 7). The β-spin HOMO−LUMO gap (4.4 eV) in the Mn complex is the second largest (the Zn complex has the largest HOMO−LUMO gap in the series).

In the Fe complex, with one more valence electron, the lowest of the d orbitals (d$_{yz-xz}$) is the HOMO, and it is stabilized by 4.4 eV, relative to the analogous orbital in [MnL(SC$_6$F$_5$)]. The β-HOMO−LUMO gap becomes smaller, 3.7 eV, reflecting a larger Z_{nuc}^{eff} value for Fe relative to that of Mn (vide supra). The increased Z_{nuc}^{eff} shifts the energies of metal-based orbitals closer to the occupied thiolate ligand orbitals and increases the covalent contribution to metal−thiolate bonding (Table 2).

In the Co complex, the next d orbital (d$_{yz+xz}$) becomes occupied. Because the value of Z_{nuc}^{eff} for Co is greater than that of Fe, the β-HOMO−LUMO gap again becomes smaller (3.2 eV) and the covalency of the metal−thiolate bond is further increased (Table 2). The important contribution comes from HOMO-5, which is a bonding combination of the S(thiolate) pσ orbital (HOMO-1 of SC$_6$F$_5^-$) and Co d$_{xy}$. The largest HOMO-5 contribution to M−S bond order indicates the strongest σ bonding component among all [ML(SC$_6$F$_5$)] complexes.
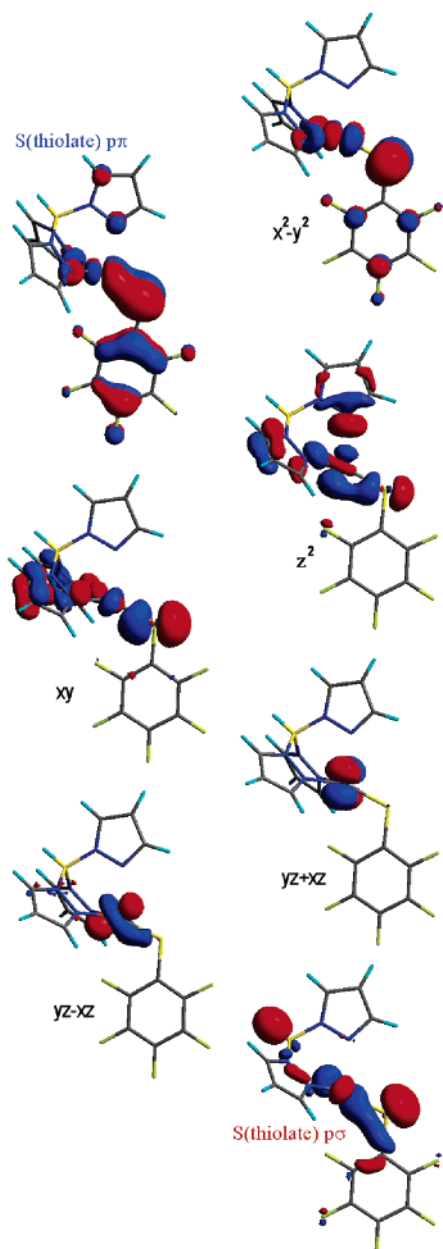
Figure 8. Contour surfaces of frontier molecular orbitals of the [ML-(SC$_6$F$_5$)] complexes.

In the Ni complex, the d$_{xy}$ orbital is occupied. This cancels the S(thiolate) pσ–M d$_{xy}$ bonding component for the covalent M–S bond and causes the overall M–S bond order to decrease (section 4.4). Because the d$_{xy}$ orbital is now below the S(thiolate) pσ orbital (Figure 7), the latter is destabilized by ~1 eV. The greater Z_{nuc}^{eff} for Ni results in a further lowering of the energies of M 3d-based orbitals and favors the more efficient covalent bonding with the S(thiolate) pπ orbital. As a result, the S character in the LUMO (d$_{x^2-y^2}$) is increased to 8%, and the corresponding HOMO (SC$_6$F$_5^-$) contribution is 12%.

In the Cu complex, the d$_{z^2}$ orbital is populated and the Cu d$_{x^2-y^2}$ is the only unoccupied d orbital. As a result of the still larger Z_{nuc}^{eff}, the β-HOMO–LUMO gap for [CuL-(SC$_6$F$_5$)] is the lowest (2.4 eV), maximizing the orbital interaction between the S(thiolate) pπ and Cu d$_{x^2-y^2}$. The
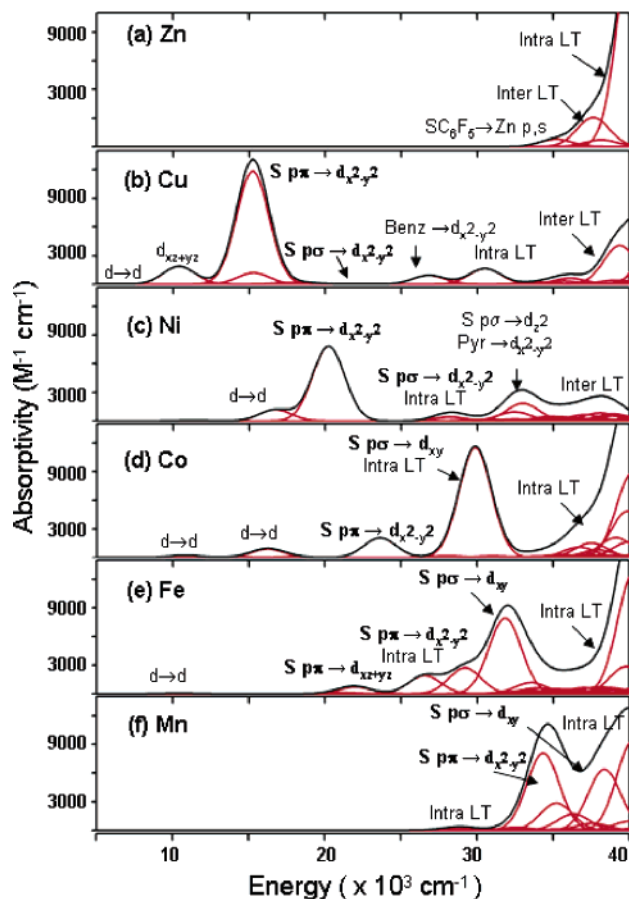
Figure 9. Simulated electronic spectra of [ML(SC$_6$F$_5$)] from the TDDFT calculations. The contributions from individual electronic transitions are shown in red.

β-HOMO of the complex is composed of 49% of HOMO-(SC$_6$F$_5^-$) and 41% β-LUMO(ML$^+$) and the β-LUMO of the complex, which is the antibonding counterpart of the β-HOMO, is composed of 39% of HOMO (SC$_6$F$_5^-$) and 44% of β-LUMO (ML$^+$) (Figure S3). Alternatively, the S character of the β-LUMO is 27%, and the Cu 3d character of the β-HOMO is 21%. Thus, the β-HOMO/LUMO compositions in the Cu complex indicate the most covalent M–S bond in the series and the largest charge transfer from the thiolate to the metal (Table 2).

In the Zn complex, all of the d orbitals of the metal ion are occupied, including the Zn d$_{x^2-y^2}$–S pπ orbital. Thus, the π contribution to covalency is canceled, and the covalent bonding interactions between the Zn 3d orbitals and the thiolate orbitals become very small; the charge transfer from the thiolate to the metal is the smallest in the series (Table 2). The only remaining covalent interactions come from the Zn 4s,4p orbitals (Figure S4 in Supporting Information). Note that the amount of M 4s,4p–thiolate mixing changes little (26.2–32.5%, Table 2) over the [ML(SC$_6$F$_5$)] series.

4.3. TDDFT Calculations of Electronic Spectra. Figure 9A–F presents the calculated absorption spectra (5000 to 40 000 cm^{-1}) for the [ML(SC$_6$F$_5$)] complexes and lists the principal electronic excitations which contribute to the electronic transitions. In the spectrum of the Zn complex (Figure 9A), there are no transitions in the 5000–30 000 cm^{-1} region, consistent with the experimental UV–vis

absorption data (Figure 2). This is the result of the filled d^{10} electronic configuration in the Zn(II) ion. The higher-energy region ($>35\,000$ cm^{-1}) exhibits some absorption intensity ($\epsilon \approx 1000$ M^{-1} cm^{-1}) because of the S(thiolate) p$\pi \rightarrow$ Zn 4p transition, the S(thiolate) p$\pi \rightarrow$ (pyrazolyl) π interligand transition, and the benzyl-based intraligand charge-transfer transitions.

The primary feature of the TDDFT calculated spectrum of the copper complex (Figure 9B) is the intense absorption at $\sim$15 000 cm^{-1} from the S(thiolate) p$\pi \rightarrow$ Cu d$_{x^2-y^2}$ (β-spin HOMO $\rightarrow$ LUMO) transition. It is characteristic of copper complexes to have the highly covalent S(thiolate) pπ−Cu interaction in the ground state, and this leads to their blue color.[1−3] In the lower-energy (5000−12 000 cm^{-1}) region, the four LF transitions are in the following order: d$_{z^2}$ < d$_{xy}$ < d$_{xz+yz}$ < d$_{xz-yz}$. Note that one of the LF transitions (d$_{xz+yz} \rightarrow$ d$_{x^2-y^2}$) gains absorption intensity by mixing with the allowed S(thiolate) p$\pi \rightarrow$ Cu d$_{x^2-y^2}$ LMCT transition, as observed. In the higher-energy region, TDDFT predicts two weak (pyrazolyl) p$\pi \rightarrow$ Cu d$_{x^2-y^2}$ CT transitions at 15 300 and 17 600 cm^{-1}. The S(thiolate) p$\sigma \rightarrow$ Cu d$_{x^2-y^2}$ LMCT excitation is at 23 000 cm^{-1} with very little intensity. The absorption intensity at 27 000 and 30 000 cm^{-1} is the result of thiolate p$\pi \rightarrow$ Cu d$_{x^2-y^2}$ and thiolate-based intraligand transitions, respectively. The interligand CT transitions have absorption intensities in the $>37\,000$ cm^{-1} region. The calculated spectrum is in very good agreement with the experimental absorption data (Figure 2) and the past band assignments for Cu−thiolate complexes[1,57] (section 3.1).

The calculated absorption spectrum of the Ni complex (Figure 9C) exhibits a dominant feature at $\sim$20 000 cm^{-1} which is the result of the S(thiolate) p$\pi \rightarrow$ Ni d$_{x^2-y^2}$ LMCT transition. This transition is higher in energy (from 15 000 to 20 000 cm^{-1}) and lower in intensity (from 12 000 M^{-1} cm^{-1} to 8000 M^{-1} cm^{-1}) compared to the corresponding transition (S(thiolate) p$\pi \rightarrow$ Cu d$_{x^2-y^2}$) in the Cu complex (Figure 9B) as observed experimentally (Figure 2) and as expected from the decreased β-spin HOMO (SC$_6$F$_5^-$)−LUMO (NiL$^+$) interaction (Figure 7). Ligand-field transitions (d$_{yz+xz} \rightarrow$ d$_{x^2-y^2}$ and d$_{yz-xz} \rightarrow$ d$_{z^2}$) into the two singly occupied orbitals in the ground state of Ni(II)) form the lower-energy shoulder at 16 000 cm^{-1}. In the higher-energy region ($>25\,000$ cm^{-1}), there are the S(thiolate) p$\sigma \rightarrow$ Ni d$_{x^2-y^2}$ transitions, benzyl-based intraligand CT transitions, S(thiolate) p$\sigma \rightarrow$ Ni d$_{z^2}$ transitions, and (pyrazolyl) p$\pi \rightarrow$ Ni d$_{x^2-y^2}$ transitions. Interligand CT transitions are present in the $\sim$37 000 cm^{-1} region, similar to those in the Cu complex.

Figure 9D presents the absorption spectrum for [CoL-(SC$_6$F$_5$)]. The LF transitions are calculated to be in the 10 000−20 000 cm^{-1} region. The S(thiolate) p$\pi \rightarrow$ Co d$_{x^2-y^2}$ charge-transfer transition is present at 24 000 cm^{-1} ($\epsilon \approx 3000$ M^{-1} cm^{-1}); this transition is higher in energy and lower in intensity than the corresponding band in the Ni complex (20 000 cm^{-1} and $\epsilon \approx 8000$ M^{-1} cm^{-1}) as observed experimentally. The interesting feature in the Co complex is an intense ($\epsilon \approx 11\,000$ M^{-1} cm^{-1}) S(thiolate) p$\sigma \rightarrow$ Co d$_{xy}$ charge-transfer transition at 30 000 cm^{-1}. In Co(II) the

additional, relative to Ni(II), singly occupied orbital is the d$_{xy}$ orbital (Figure 8) which has a σ interaction with the S(thiolate), and this leads to the intense absorption at 30 000 cm^{-1}. This reverses the pattern of more intense S(thiolate) pπ and less intense S(thiolate) pσ to M d$_{x^2-y^2}$ orbital CT transitions observed in the Cu and Ni complexes to show a less intense S(thiolate) p$\pi \rightarrow$ M d$_{x^2-y^2}$ transition and a more intense S(thiolate) p$\sigma \rightarrow$ M d$_{xy}$ transition. This behavior explains the spectral differences in Figure 2 in which the absorption intensity at $\sim$30 000 cm^{-1} from the S(thiolate) pσ LMCT transition is more intense than the transition at $\sim$25 000 cm^{-1} from the S(thiolate) pπ LMCT transition. There are SC$_6$F$_5$-based intraligand excitations contributing to the absorption intensity, similar to the other metal−thiolate complexes in the higher-energy region ($>35\,000$ cm^{-1}).

The TDDFT calculated spectrum for the Fe complex (Figure 9E) shows low-intensity ligand-field transitions in the 5000−20 000 cm^{-1} region. The S(thiolate) p$\sigma \rightarrow$ Fe d$_{xy}$ LMCT excitation appears as the intense absorption ($\epsilon \sim 8000$ M^{-1} cm^{-1}) at 32 000 cm^{-1}, compared to the less intense ($\epsilon \sim 2200$ M^{-1} cm^{-1}) S(thiolate) p$\pi \rightarrow$ Fe d$_{x^2-y^2}$ CT excitation contributing to the absorption intensity at $\sim$28 000 cm^{-1}. Intraligand transitions also contribute to absorption intensity in this energy region. The S(thiolate) p$\sigma \rightarrow$ Fe d$_{xy}$ LMCT transition is higher in energy (by 2000 cm^{-1}) and lower intensity (by 3000 M^{-1} cm^{-1}) and the S(thiolate) p$\pi \rightarrow$ Fe d$_{x^2-y^2}$ LMCT transition is also higher in energy (by 4000 cm^{-1}) and lower in intensity (by 800 M^{-1}cm^{-1}) relative to the corresponding excitations in the Co complex (vide supra, particularly the data in Figure 2). This is a reflection of the lower M 3d−S(thiolate) covalency upon changing from Co to Fe.

The [MnL(SC$_6$F$_5$)] complex does not have significant absorption intensity in the 5000−25 000 cm^{-1} region. This is because the LF transitions in high-spin Mn(d^5) complexes are both spin and Laporté forbidden.[56] The absorption intensity at $\sim$35 000 cm^{-1} is the result of the S(thiolate) p$\pi \rightarrow$ Mn d$_{x^2-y^2}$ LMCT transition, and the one at 38000 cm^{-1} is the result of the S(thiolate) p$\sigma \rightarrow$ Mn d$_{xy}$ LMCT transition. Intraligand CT transitions are present at higher energy ($\sim$40 000 cm^{-1}).

Thus, the calculated electronic absorption spectra are in good agreement with the experimental spectra for the [ML-(SC$_6$F$_5$)] complexes. First, the zinc and manganese complexes with d^{10} and d^5 electronic configurations do not exhibit absorption in the 5000−30 000 cm^{-1} region. Second, in going from the copper to iron (Cu $\rightarrow$ Ni $\rightarrow$ Co $\rightarrow$ Fe) complexes, the S(thiolate) p$\pi \rightarrow$ M d$_{x^2-y^2}$ CT transition shifts to higher energy and decreases in intensity. Third, the Co complex exhibits a reversal in the π/σ intensity ratio compared to that of the Cu and Ni complexes. In going from Co to Fe, the S(thiolate) p$\sigma \rightarrow$ M d$_{xy}$ CT transition shifts to higher energy and decreases in intensity.

4.4. Trends in Metal−Thiolate Bonding. From the bond order analysis, the metal−sulfur bonding is a dominant interaction between the ML$^+$ fragment and the thiolate ligand contributing 75−81% to the total bond order between the two molecular fragments (Figure 10A). The M−S bond order
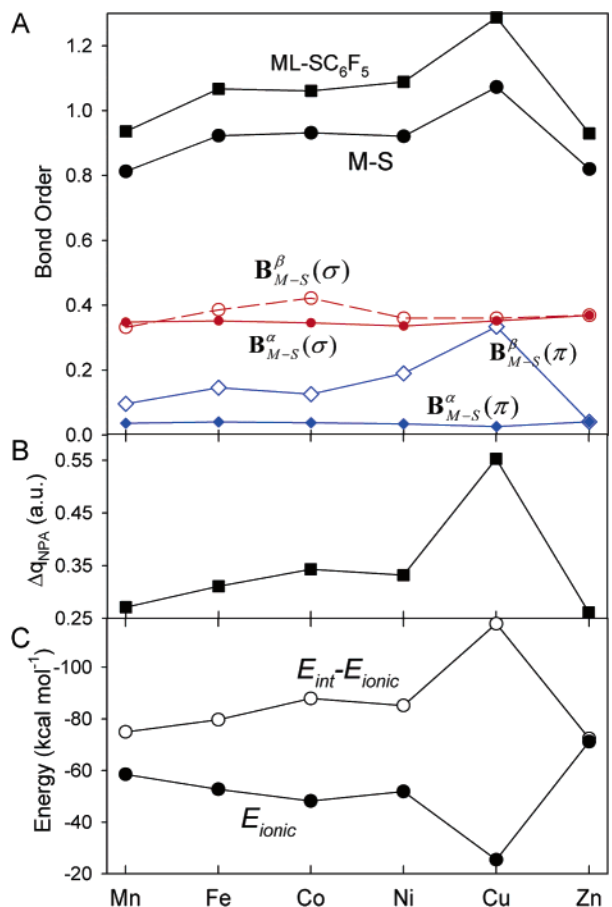
Figure 10. (A) Mayer M−S bond order (solid black circles), its σ and π components (in red and blue, respectively), and the bond order between the ML^+ and $SC_6F_5^-$ fragments (solid black squares) in the $[ML(SC_6F_5)]$ complexes. (B) Charge donation from the $SC_6F_5^-$ ligand to the ML^+ fragment. (C) Ionic component of the $ML^+-SC_6F_5^-$ bonding energy, E_{ionic}, and the difference, $E_{int} - E_{ionic}$.

(and the total $ML-SC_6F_5$ bond order) in the $[ML(SC_6F_5)]$ complexes follows the Mn < Fe < Co > Ni < Cu > Zn progression found in the M−S force constants (Figure 6) and the charge transfer from the $SC_6F_5^-$ ligand to the ML^+ fragment (Table 2, Figure 10B).

It is possible to use symmetry-adapted orbitals in the bond-order analysis to gain additional insight. The σ bond component to the Mayer bond orders from the α-spin MOs, $B^{\alpha}_{M-S}(\sigma)$, is fairly constant through the series. This is because the α-spin LUMO of the ML^+ fragment (this orbital has 75−80% M 4s and 25−30% M 4p character) remains relatively unperturbed (in its energy and composition) by the nature of the central atom.

As a result, the coupling between the α-spin LUMO of the ML^+ fragment and the HOMO-1 of the $SC_6F_5^-$ fragment remains similar for all of the complexes in this series.

All α-spin metal 3d-based orbitals are occupied and cannot contribute to covalent bonding with the thiolate ligand donor orbitals. Thus, the π component to the bond orders from the α-spin MOs, $B^{\alpha}_{M-S}(\pi)$, is close to zero. Zn(II) has a filled d^{10} shell, so its α- and β-spin orbital contributions to bond orders are equal, and the M−S bond covalency is limited to the Zn 4s,4p−thiolate $p\sigma$ orbital interactions.

The B^{α}_{M-S} indices provide a useful baseline for observing changes in β-spin MO σ and π contributions to the bond orders. As discussed in section 4.2, the increasing Z^{eff}_{nuc} (from Mn(II) to Zn(II)) results in the stabilization of the M 3d-based molecular orbitals and makes the M 3d−thiolate covalency stronger, given that the electron occupancy of the appropriate MOs allows the net contribution to be positive. This is the case for the σ component, $B^{\beta}_{M-S}(\sigma)$, in going from Mn(II) to Fe(II) to Co(II), and for the π component, $B^{\beta}_{M-S}(\pi)$ when proceeding from Mn(II) to Cu(II). These changes in σ and π components of the covalent bonding between the metal and thiolate produce the observed net bond order trends with a local maximum at Co(II) and a global maximum at Cu(II).

If the metal−thiolate bonding in the $[ML(SC_6F_5)]$ complexes was limited to only covalent interactions, the calculated bond orders would directly correlate with the metal−thiolate bond energies and, thus, we would observe the maxima of the metal−thiolate bond energies at Co(II) and Cu(II) (notice the correlation between the M−S bond orders and $E_{int} - E_{ionic}$, Figure 10). However, this is not the case (Figure 6). While the Co complex shows the second largest metal−thiolate binding energy, the absolute maximum is observed for the Zn complex, not for the Cu complex. This indicates that the ionic contribution, along with the covalent component of the bond energy, plays an important role in determining the overall strength of the metal−thiolate interaction (Figure 10C): ∼44% ionic/56% covalent in Mn(II), becoming more and more covalent (with maxima at Co(II) for σ-type bonding and at Cu(II) for π-type bonding), and back to ∼50% ionic/50% covalent in Zn(II).

5. Discussion

Important spectral trends are observed in the series of metal−thiolate model complexes $[ML(SC_6F_5)]$ both experimentally and computationally (TDDFT). The intense S(thiolate) $p\pi \rightarrow$ M $d_{x^2-y^2}$ (M = Cu, Ni, Co, and Fe) charge-transfer transition shifts to higher energy proceeding from Cu $\rightarrow$ Ni $\rightarrow$ Co $\rightarrow$ Fe. The intensity of this charge-transfer transition decreases along the series, Cu $\rightarrow$ Ni $\rightarrow$ Co $\rightarrow$ Fe, because of the reduced M 3d−thiolate covalency, supported by the decrease in the pre-edge intensity in the S K-edge XAS data and in the MO calculations. An important feature is observed in the cobalt complex, the S(thiolate) $p\sigma \rightarrow$ Co d_{xy} charge-transfer transition is now present and more intense relative to the S(thiolate) $p\pi \rightarrow$ Co $d_{x^2-y^2}$ charge-transfer transition. This is consistent with its ground-state electronic structure description (from the DFT calculations) indicating the strong interaction between the Co d_{xy} and the S(thiolate) $p\sigma$ orbitals. Similar to the trend in the S(thiolate) $p\pi \rightarrow$ M $d_{x^2-y^2}$ CT transition, the S(thiolate) $p\sigma \rightarrow$ M d_{xy} CT transition shifts to higher energy and decreases in intensity upon changing from Co to Fe to Mn.

Trends in the metal−thiolate bonding were evaluated using DFT methods to obtain insight into the variation in the observed spectral features from the different metal−thiolate interactions in these complexes. These calculations indicate

that the observed variations in geometry, spectra, and bond energies of the metal−thiolate complexes can be explained by changes in the nature of metal−thiolate interactions.

5.1. Covalent Bonding. The covalent bonding due to the metal 4s,4p−thiolate interactions is dominant in this metal−thiolate series, and its strength remains approximately the same over the series. This is reflected by the σ bond component of the bond orders from the α-MOs, $B_{M-S}^{\alpha}(\sigma)$ (Figure 10A) and the observation that the α-spin-occupied molecular orbitals of each [ML(SC$_6$F$_5$)] complex contain 26−32% of the unoccupied molecular orbitals of the ML$^+$ fragment (Table 2).

Additional small σ-bond and larger π-bond contributions to the covalent bonding are the result of M d$_{xy}$−pσ thiolate and M d$_{x^2-y^2}$−pπ thiolate orbital interactions, respectively. These additional interactions grow stronger when going from Mn(II) to Co(II) (the σ contribution) and to Cu(II) (the π contribution). The observed changes in the d(M)−thiolate orbital interactions are caused by a monotonic increase of the effective nuclear charge of the metal atom upon going from Mn(II) to Zn(II) and the increasing electron population of β-spin 3d orbitals (d^5 → d^{10}). The higher effective nuclear charge of the metal atom brings the energies of the d$_{xy}$ and d$_{x^2-y^2}$ orbitals of the metal atom closer to the thiolate-occupied orbitals and favors the covalent M 3d−thiolate interactions.

5.2. Ionic Bonding. The ionic bonding plays an important role in determining the overall strength of the ML$^+$−SC$_6$F$_5^-$ interaction. It contributes ∼44% and 50% to the ML$^+$−SC$_6$F$_5^-$ bond energy in Mn(II) and Zn(II), respectively (Figure 10C).

The higher effective nuclear charge of the metal atom favors covalent metal−thiolate interactions, but it also causes a decrease in the metal ionic radii. The latter would cause a gradual increase in the ionic component of the ML$^+$−SC$_6$F$_5^-$ bond energy in going from Mn(II) to Zn(II) if the M−S covalency remained the same. However, this effect is obscured by the changes in the M−S covalency which result in charge donation from the thiolate ligand to the ML$^+$ fragment (Figure 10B). Thus, the covalency causes the metal charge to decrease to less positive values and the sulfur charge to become less negative (Figure 6D) thus reducing the ionic component of the M−S bond energy (Figure 10C). Thus, there is a *compensating effect*: as the covalent contribution to the metal−thiolate bonding increases, the ionic contribution decreases. An important implication for the [ML(SC$_6$F$_5$)] complexes is that the metal−thiolate binding energy shows little variation over this series. The two metal−thiolate complexes, [CuL(SC$_6$F$_5$)] and [ZnL(SC$_6$F$_5$)], have similar metal−thiolate bonding parameters (E_o, k, d_{M-S}), yet only [CuL(SC$_6$F$_5$)] shows a very intense low-energy CT band reflecting the high covalency of the cupric complex which is not present in the zinc complex.

5.3. Periodic Trends. As discussed above, the character of the metal−thiolate bond becomes more covalent, going from Mn(II) to Cu(II), reaching the maxima at Co(II) and Cu(II). As a result, the metal−sulfur bond length decreases from 2.39 Å for Mn to 2.18 Å for Cu and the force constant

increases from 1.13 to 1.43 mDyne Å^{-1}. The other parameters of the metal−thiolate bond, E_o and E_{int}, show a trend toward greater binding as we move from Mn to Zn. However, the fine structure of the binding-energy curve (Figure 6) is more complex because E_{int} is the sum of two contributions which are linked through charge transfer and compensate each other (Figure 10C).

The metal−thiolate force constant is very similar in [CuL(SC$_6$F$_5$)] and [ZnL(SC$_6$F$_5$)]. The Zn complex shows a longer M−S bond distance than the Cu complex; however, the calculated metal−thiolate interaction energy in the Zn complex is 2 kcal mol^{-1} stronger than it is in the Cu complex with the largest M−S covalency. For the Zn complex, the M 3d−thiolate covalency is lost (all 3d orbitals are occupied) and the remaining M 4s,4p−thiolate covalency contributes only ∼50% to the metal−thiolate interaction energy. The large ionic contribution compensates for the lost M−S covalency and results in the strongest metal−thiolate bond in this series (Figures 6B and 10). The lack of a correlation between bond strength and length (see Figure 6) for the Cu and Zn complexes reflects the differences in the distance dependence of the ionic versus covalent contributions to bonding. In such a case, the general correlation of the bond energy, length, and force constant does not hold.

5.4. Irving−Williams Series. If the successive stability constants of complexes of divalent ions of the first transition series are plotted against the atomic number of the element, there is a monotonic increase to a maximum at Cu regardless of the nature of the ligand.[16−18] This order was explained by Irving and Williams[17] as a consequence of the fact that the two parameters, which serve as a guide to the magnitude of the ionic (electrostatic) and covalent interactions (the reciprocal of the metal ionic radius and the sum of the first two ionization energies, respectively), both increase monotonically throughout the series from Mn to Cu and then decrease from Cu to Zn. Thus, if water is replaced from [M(OH$_2$)$_n$]$^{2+}$ by a ligand of better electron-donating power, the gain in stability will increase with the ionization potential of the metal. If H$_2$O is replaced by a ligand with a formal negative charge, the stability gain through electrostatic forces will increase as the radius of the metal cation decreases.

Figure 6B shows that the metal−thiolate binding energies in [ML(SC$_6$F$_5$)] do not show the trend expected for the Irving−Williams series. The calculated binding energy varies from −126.8 kcal mol^{-1} for Mn to −130.8 kcal mol^{-1} for Cu and to −132.7 kcal mol^{-1} for Zn. As discussed in section 5.2 and as is shown in Figure 10C, this is a result of the compensating effect in the metal−thiolate complexes where the covalent contribution to bonding is comparable in magnitude to the ionic contribution to bonding.

To explain the Irving−Williams series, we have also analyzed the metal−ligand bonding in a series of [ML(F)] (where L = HB(pz)$_3^-$) complexes where the fluoride models the fourth ligand being replaced by the thiolate. Our analysis indicates that the metal−ligand bonding in these complexes is dominated by the ionic contribution (compare Figures 10C and 11), and the magnitude of the metal−fluoride binding energy (Figure S5) decreases from −176.4 kcal mol^{-1} for
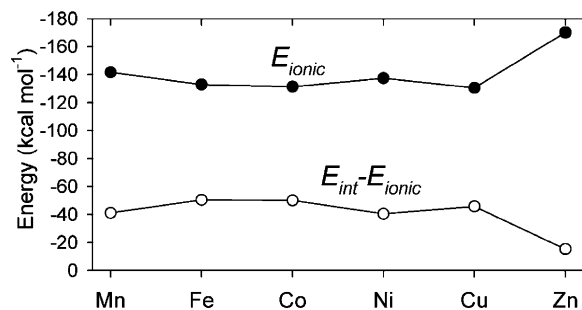
Figure 11. Ionic component of the ML^+-F^- bonding energy, E_{ionic}, and the difference, $E_{int} - E_{ionic}$, in the [ML(F)] complexes.

Mn to -166.1 kcal mol^{-1} for Cu and then increases to -176.6 kcal mol^{-1} for Zn. This variation in the binding energy is a result of the increasing metal−ligand covalency going from Mn to Cu which reduces the ionic interaction (Figures S6 and S7).

However, because of the dominant ionic contribution to bonding in the [ML(F)] series, the compensating effect of the increasing covalent bonding contribution is not as large as in the [ML(SC$_6$F$_5$)] series. As a result, the difference between the relative formation energies of the metal−thiolate complexes and the metal−fluoride complexes

$$\Delta E_f = [E_o(ML^+-SC_6F_5^-) - E_o(MnL^+-SC_6F_5^-)] - $$
$$[E_o(ML^+-F^-) - E_o(MnL^+-F^-)]$$

shows the Mn $\approx$ Fe > Co > Ni > Cu < Zn progression (Figure 11) which is the Irving−Williams series. Moreover, the stability constants of the metal−thiolate complexes calculated from the binding-energy differences are consistent with the experimentally observed quantities.[16−18]

Thus, the "softer" thiolate ligand can have comparable covalent and ionic contributions to bonding, and these compensate to produce little change in the binding energy over the series of metal ions (open squares in Figure 12). For the "harder" ligands (F$^-$, OH$^-$, H$_2$O, etc.), the ionic term
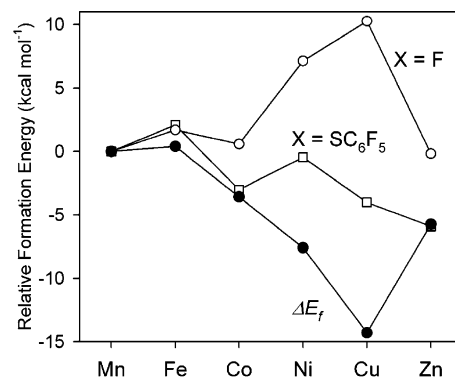

Figure 12. Relative formation energies (kcal mol^{-1}) of the metal−thiolate complexes, [ML(SC$_6$F$_5$)], and the metal−fluoride complexes, [ML(F)], and their difference, ΔE_f.

dominates and their binding energies are affected by changes in covalency over the series (open circles in Figure 12). It is the competition between these behaviors that produces the Irving−Williams series (solid circles in Figure 12) in stability constants.

Supporting Information Available: Listings of the optimized structures, a summary of calculated electronic parameters, calculated IR spectra, the rR spectrum of [NiL(SC$_6$F$_5$)] (excitation wavelength $\lambda_o = 351$ nm), and the molecular orbital interaction diagrams for [CuL(SC$_6$F$_5$)] and [ZnL(SC$_6$F$_5$)]. This material is available free of charge via the Internet at http://pubs.acs.org.

IC050371M